

Hybrid High-Voltage $\text{LiNi}_{0.5}\text{Mn}_{1.5}\text{O}_4$ /Graphite Cathodes Enabling Rechargeable Batteries with Simultaneous Anion- and Cation Storage

Sven Künne,^{*[a]} Jakob Michael Hesper,^[a] Tobias Lein,^[b] Karsten Voigt,^[b] Daria Mikhailova,^[c] Alexander Michaelis,^[b, d] Martin Winter,^[a, e] Tobias Placke,^[a] and Christian Heubner^{*[d]}

A hybrid cathode concept that targets combining the specific advantages of Li-ion batteries and dual-ion batteries is proposed. $\text{LiNi}_{0.5}\text{Mn}_{1.5}\text{O}_4$ (LNMO), (de)inserting Li^+ , and graphite, capable to (de)intercalate PF_6^- present in the electrolyte, are combined in one cathode, aiming for synergy effects due to the presence of two electrochemically active species to overcome rate limitations caused by electrolyte depletion. Hybrid cathodes of different compositions and designs are prepared and investigated regarding their properties and the storage mechanism using electrochemical analyses combined with *operando*

XRD and extensive materials characterization, including scanning electron microscopy and energy-dispersive X-ray spectroscopy. Finally, hybrid cathodes with higher areal capacity are prepared and investigated regarding rate performance. Model-based analysis of the results reveals design criteria and material properties required to achieve synergistic effects between the components in hybrid cathodes. These insights lay the foundation for a new type of battery with advantageous properties in terms of cost, environmental friendliness, and electrochemical performance.

Introduction

The development of reliable, safe and at the same time powerful and cost-effective battery technologies is a key element for sustainable mobility and energy supply. However, the increased use of batteries requires measures to conserve resources and increase energy efficiency. Currently, rechargeable lithium ion batteries (LIBs) dominate the battery market for

mobile electronic devices as well as for battery electric vehicle (BEV) operation and for home and grid storage applications.^[1] However, efforts are still needed to improve energy and power density, fast-charging capability, safety and lifetime, as well as to reduce manufacturing costs and enable full recyclability.^[2] State-of-the-art cathode materials for LIBs are LiFePO_4 and layered transition metal oxides (e.g., $\text{LiNi}_x\text{Co}_y\text{Mn}_z\text{O}_2$; NCM), while there are other promising candidates for next-generation low-cost LIB cells such as the high-voltage spinel $\text{LiNi}_{0.5}\text{Mn}_{1.5}\text{O}_4$ (LNMO).^[3] Graphite and graphite/silicon(oxide) blends are commonly used as anodes.^[4] Current research and development address the development of advanced cathode and anode materials that enable higher specific capacity or higher cell voltage with suitable lifetime, that have lower costs. Another approach to increase the energy density at cell level is to optimize the electrode design. In particular, increasing the amount of active material within the electrodes notably increases the volumetric and gravimetric energy density,^[5] which can be achieved by increasing the coating thickness and reducing the porosity, thus increasing the electrode density.^[6] However, due to the increasing limitation of Li^+ ion transport in the electrolyte within the electrode pores for thick electrodes, these measures can lead to a reduction in power density and fast-charging capability.^[7–9] Sufficient power density and fast-charging capability are, however, mandatory for the operation of demanding applications, such as BEVs or power tools.^[10]

Dual-ion batteries (DIBs) are a novel battery technology that can meet various key requirements, such as long lifetime, low cost and easy recyclability.^[11–14] The cell chemistry and charge-discharge storage mechanism of DIBs differs from conventional LIBs. For DIBs, the Li^+ -cation-supplying cathode is replaced by an anion-storage material, while the salt in the electrolyte is considered as active material and provides both the cations and

[a] S. Künne, J. M. Hesper, Prof. M. Winter, Dr. T. Placke

University of Münster,
MEET Battery Research Center
Institute of Physical Chemistry
Corrensstraße 46, 48149 Münster (Germany)
E-mail: sven.kuenne@uni-muenster.de

[b] T. Lein, K. Voigt, Prof. A. Michaelis
Institute of Materials Science
TU Dresden
01062 Dresden (Germany)

[c] Dr. D. Mikhailova
Leibniz Institute for Solid State and Materials Research (IFW) Dresden e.V.
Institute for Complex Materials
Helmholtzstraße 20 01069 Dresden (Germany)

[d] Prof. A. Michaelis, Dr. C. Heubner
Fraunhofer Institute for Ceramic Technologies and Systems IKTS
Winterbergstraße 28, 01277 Dresden (Germany)
E-mail: christian.heubner@ikts.fraunhofer.de

[e] Prof. M. Winter
Helmholtz-Institute Münster
IEK-12, Forschungszentrum Jülich GmbH
Corrensstraße 46, 48149 Münster (Germany)

Supporting information for this article is available on the WWW under <https://doi.org/10.1002/batt.202300284>

© 2023 The Authors. *Batteries & Supercaps* published by Wiley-VCH GmbH. This is an open access article under the terms of the Creative Commons Attribution License, which permits use, distribution and reproduction in any medium, provided the original work is properly cited.

anions to be stored simultaneously in both electrodes. Graphite is widely used as cathode material in DIBs due to its layered structure enabling reversible anion storage, environmentally friendliness, and low cost. During the charging process, cations (e.g., Li⁺, K⁺, etc.) are inserted into or deposited on the anode (e.g., graphite or Li/K metal), while at the same time anions (e.g., PF₆⁻) are intercalated into the graphite cathode.^[13] During discharging, the cations and anions are transported back into the electrolyte. The intercalation of anions on the graphitic cathode enables high cell voltages of up to 5.2 V, which is favorable to achieve high energy density. The usage of abundant and environmentally benign cathode materials and the possibility to use other active cations (e.g., Na⁺, K⁺, Zn²⁺, Al³⁺) based electrolytes enables a further reduction of overall cost and environmental pollution. Strategies for optimizing DIBs are based on two main approaches, i.e., (1) the optimization of the electrolyte and (2) the development of host materials with high-voltage stability and high anion storage capacity.^[15] Although enormous progress has been made in recent years, e.g., anion storage capacities of up to 170 mAh g⁻¹,^[16] cycling stability of up to 25,000 cycles and high rate capability,^[17] DIBs are still in a rather early research and development stage (low technology readiness level (TRL)) compared to LIBs.^[18] Most notably, current Li-based DIBs at the lab-scale have rather low energy density due to both, unsatisfactory active material content in the electrodes, low areal specific capacities and the relatively low density of graphite. Besides their different TRLs, obviously, LIBs and DIBs each have their specific advantages, but also suffer from individual drawbacks. Herein, we propose a hybrid high-voltage LiNi_{0.5}Mn_{1.5}O₄/graphite (LNMO/Gr) cathode concept that targets combining the specific advantages of LIBs and DIBs, suppressing the respective disadvantages, and aiming for synergy effects due to the presence of two electrochemically active host materials and two ionic storage species (Li⁺ and PF₆⁻). A schematic drawing and the motivation behind the working principle of a cell containing the LNMO/Gr hybrid cathode and the corresponding LNMO/Gr || Li metal cell is shown in Figure 1.

Recently, Hao *et al.*^[19] reported an LiFePO₄ (LFP)/graphite hybrid cathode for Li⁺ and PF₆⁻ storage, however, these materials exhibit completely separated operating potentials, i.e., <4.0 V vs. Li|Li⁺ for Li⁺ extraction/insertion into LFP and >4.5 V vs. Li|Li⁺ for PF₆⁻-intercalation/de-intercalation into graphite. In our work and for the purpose of simultaneous storage of anions and cations within a similar potential range at the cathode (>4.5 V vs. Li|Li⁺), the high-voltage spinel LNMO cathode material from LIB technology is combined with graphite, which is typically used in DIB cathodes. During charging of the LNMO/Gr||Li metal cell, Li⁺ ions are removed from LNMO [Equation (1)] and at the same time electrolyte anions (e.g., PF₆⁻) are incorporated into the graphite [Equation (2)], while Li⁺ ions are also deposited at the Li metal anode [Equation (3)]. These processes are reversed during discharging.

Hybrid LNMO/Gr cathodes were prepared by a standard electrode paste coating, drying, calendering procedure followed by extensive material/electrode characterization including XRD, Raman spectroscopy, SEM and EDS. The working mechanism of the hybrid cathode is investigated by advanced electrochemical analyses, *operando* XRD and *in situ* Raman spectroscopy. Electrochemical characterization and battery testing are carried out for different compositions and electrode designs. The results are supported by straightforward modelling of the rate capability and energy density estimations.

Results and Discussion

Initial characterization of LNMO/Gr hybrid cathodes

Constant current cycling of LNMO and graphite electrodes as well as hybrid cathodes was conducted in cathode || Li metal two-electrode coin cells. Figure 2 depicts the voltage vs. capacity and discharge capacity vs. cycle number plots of cells employing a state-of-the-art carbonate-based LIB electrolyte (base electrolyte, BE). Pure LNMO demonstrates the typical voltage profile, showing the plateaus related to manganese and

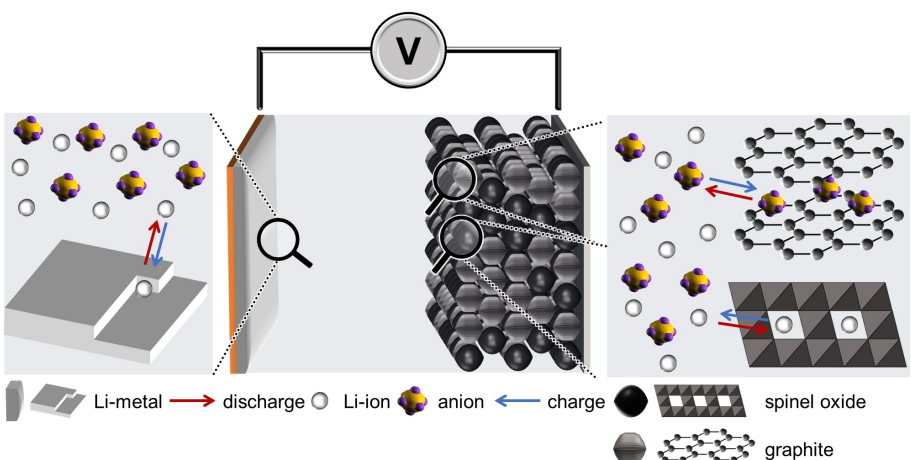


Figure 1. Schematic presentation of the storage mechanism of hybrid LNMO/Gr cathodes. Illustration of the proposed operating principle of a battery with a hybrid LNMO/Gr cathode. See text for further explanations.

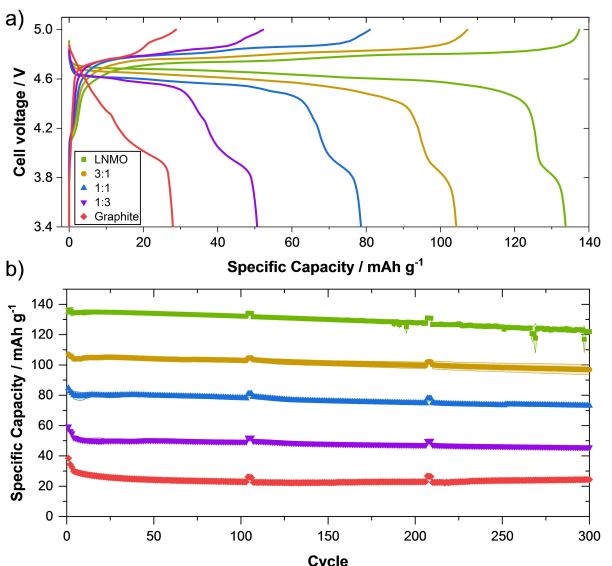


Figure 2. a) Cell voltage profiles (10th cycle) and b) specific discharge capacities from constant current charge/discharge cycling of two-electrode coin cells (cathode || Li metal) with LNMO, graphite, and the three different LNMO/graphite hybrid cathodes. Electrolyte: BE. Cell voltage range: 3.4–5.0 V. Charge/discharge rate: 0.1 C (cycles 1–3, 104–106, 207–209), 0.5 C from 4th cycle ($1\text{C} \doteq 100\text{--}147\text{ mAh g}^{-1}$).

nickel redox couples during Li^+ -insertion and extraction.^[20] The voltage profile during charging of pure graphite indicates that PF_6^- intercalation starts at above 4.6 V, characterized by two plateaus, which corresponds to the well-known staging mechanism.^[21,22] The staging mechanism of graphite intercalation compounds (GICs) is described as the ordering of the occupied galleries and the adjacent graphene layers along the c-axis, which is further discussed below.^[23,24] The stage number (n) describes the amount of graphene sheets between each intercalated layer leading to a maximum stage number of one. The co-existence of 2 stages (first order phase transition) is characterized by a potential plateau. Accordingly, the voltage profile of graphite during charging (Figure 2a) indicates that stage 2 is reached in this case.^[14] As expected, the voltage profiles of the hybrid cathodes represent features of both components, including the plateaus of manganese and nickel redox couples during Li-insertion/extraction in/from LNMO and additional shoulders for PF_6^- (de)intercalation at 4.6 V and 4.3 V.

The discharge capacities at 0.5 C in the 10th cycle of the hybrid cathodes [105 mAh g⁻¹ (3:1 LNMO/Gr), 80 mAh g⁻¹ (1:1 LNMO/Gr), 50 mAh g⁻¹ (1:3 LNMO/Gr)] roughly correspond to the sum of the capacities of the pure materials [135 mAh g⁻¹ (LNMO), 28 mAh g⁻¹ (Gr)] weighted by their mass fractions in the blend (Figure 2b). While the cycling of the LNMO || Li metal cells is quite stable, all Gr-containing electrodes and cells show substantial capacity fading varying between 2.3% and 26.2% in the first ten cycles. The initial Coulombic efficiency (ICE) ranges from 59% (Gr) to 81% (3:1), decreasing with increasing Gr-content. Upon anion intercalation – already in previous reports observed – activation barrier is likely the reason for the

onset potentials in the 1st cycle to be shifted to slightly higher potentials as in the subsequent cycles.^[12,25] A high anion intercalation potential leads to a longer exposure of the charged cathode to high potentials where the higher chance for parasitic side reactions can decrease the ICE.

Even though the results obtained with a typical LIB electrolyte demonstrate the basic functionality of the hybrid cathode, the Coulombic efficiency (C_{Eff}) and PF_6^- intercalation capacity are too low for practical applications. Therefore, a highly concentrated electrolyte (HCE) based on 4 M LiPF_6 in DMC has been investigated, as this class of electrolytes showed beneficial performance in DIBs before.^[25,26]

Figure 3 shows voltage vs. capacity and discharge capacity vs. cycle no. plots of cells employing HCE. Compared to cells using the BE, the voltage profiles of Gr and the hybrid cathodes show a more pronounced staging behavior (plateaus), indicating anion intercalation in graphite up to stage 2 (Figure 3a).^[13] The discharge capacities compared with the GIC compositions in Table S3 suggest even stage 1 formation.

The capacity rises in the first ten cycles (Figure 3b). In the case of graphite-containing electrodes, this can be explained by activation barriers that typically occur in the first cycles of anion intercalation, as well as by an insufficient wetting of the electrodes during the initial cycles.^[12,25] The specific discharge capacity (10th cycle) of LNMO is similar to cells using BE. On the contrary, all graphite-containing electrodes benefit greatly from the HCE. The pure Gr electrode delivers up to three times the discharge capacity when compared to BE. Due to the high salt concentration, the onset voltage for anion intercalation is decreased (see Figure S1) and a larger number of anions can be stored in the same voltage window.^[25] Again, the specific discharge capacities (10th cycle @ 0.5 C) of the hybrid cathodes

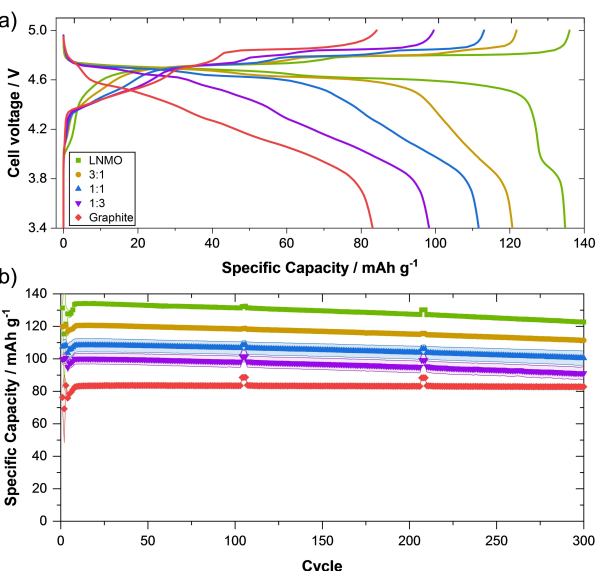


Figure 3. a) Cell voltage profiles (10th cycle) and b) specific discharge capacities from constant current charge/discharge cycling of two-electrode coin cells (cathode || Li metal) with LNMO, graphite, and the three different LNMO/graphite hybrid cathodes. Electrolyte: HCE. Cell voltage range: 3.4–5.0 V. Charge/discharge rate: 0.1 C (cycles 1–3, 104–106, 207–209), 0.5 C from 4th cycle ($1\text{C} \doteq 100\text{--}147\text{ mAh g}^{-1}$).

[121 mAh g⁻¹ (3:1 LNMO/Gr), 108 mAh g⁻¹ (1:1 LNMO/Gr), 100 mAh g⁻¹ (1:3 LNMO/Gr)] roughly correspond to the sum of the capacities of the pure materials [134 mAh g⁻¹ (LNMO), 83 mAh g⁻¹ (Gr)] weighted by their mass fraction in the blend (see Table S2). The capacity decay over 300 cycles is notably lower than for cells using the BE, which is caused by the higher oxidation stability of the HCE.^[25] Accordingly, ICE is also significantly increased when compared to the BE, ranging from 78.7% (Gr) to 88.4% (LNMO), see Table S2. The capacity retention of LNMO between the 10th and 300th cycle is 91.5% in HCE and approximately the same as in BE. In contrast, the capacity retention of Gr is significantly increased to 99.6% when using HCE. The excellent stability and higher Coulombic efficiency of Gr in HCE greatly improves the capacity retention of the hybrid electrodes, exceeding pure LNMO in the case of 3:1 (92.4%) and the 1:1 (92.6%) hybrid electrode. The 1:3 hybrid electrode shows slightly lower capacity retention of 91.1% after 300 cycles when compared to pure LNMO. This shows that the interaction of materials is more complex than a mere weighted addition of properties. Accordingly, the electrochemical behavior must be well understood in order to determine optimal compositions.

Figure 4 shows dQ/dV vs. potential plots depicting the redox activity of the materials assigned to the corresponding redox couples. For LNMO (Figure 4a) a small raise can be seen ~4.0 V vs. Li|Li⁺ that can be attributed to the oxidation of Mn³⁺ to Mn⁴⁺. Further, at 4.68 and 4.76 V vs. Li|Li⁺ peaks are observed, representing the reactions Ni²⁺|Ni³⁺ and Ni³⁺|Ni⁴⁺.^[27] Accordingly, two peaks at 4.72 and 4.65 V vs. Li|Li⁺ during discharge are shown representing the Ni reduction, while Mn reduction is observed at ~4.0 V vs. Li|Li⁺.

A constant capacity gain can be observed for the graphite electrode between 4.3 and ~4.6 V vs. Li|Li⁺ (Figure 4c) suggesting anion intercalation up to stage 3 takes place rather in a potential range than at one certain potential, corresponding to the staging mechanism mentioned before. Additional peaks are observed at 4.66 and 4.8 V vs. Li|Li⁺ with a shoulder towards 5.0 V vs. Li|Li⁺, caused by further anion intercalation at higher potentials. During discharge, a small peak at 4.76 V and a more intense peak at 4.59 V vs. Li|Li⁺ can be observed, as well as a broadening at ~4.32 V decaying towards 3.8 V vs. Li|Li⁺.

The hybrid cathodes (Figure 4b) show distinct redox peaks of both LNMO and Gr in different relative extents representing the relative active material contents. While the 3:1 hybrid cathode displays its Ni oxidation peaks at the same potentials as LNMO, the 1:1 and 1:3 hybrid cathode experience a slight shift and a small shoulder towards higher potentials which originate from the higher graphite content. Not fitting in the trend, only the 1:1 hybrid cathode shows a slight shift of the Ni reduction peaks towards higher potentials upon discharge, suggesting a beneficial influence of this particular active material ratio.

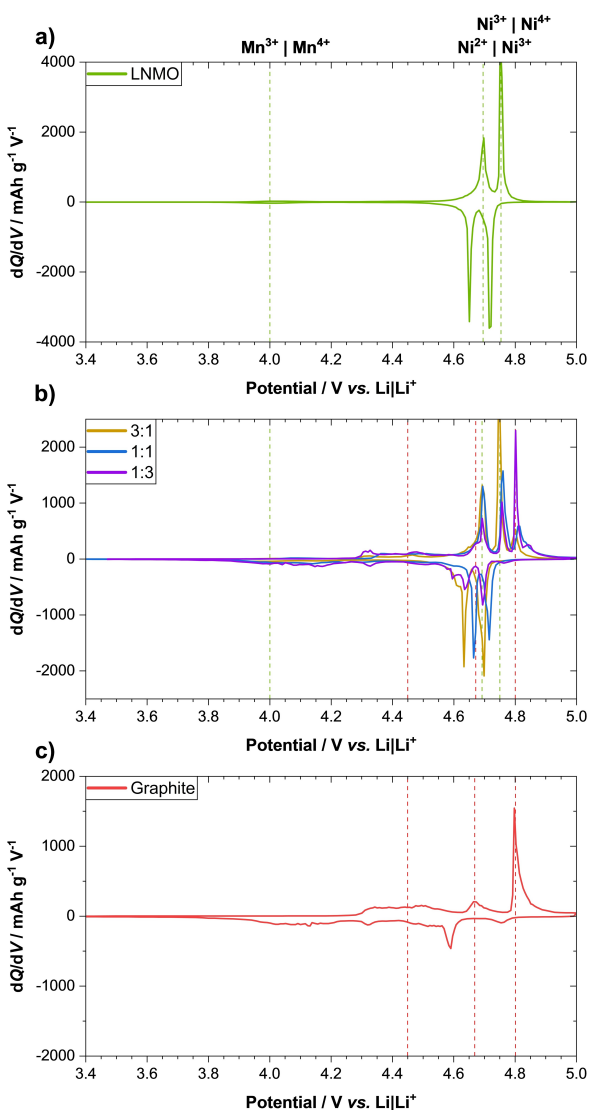


Figure 4. Differential capacity (dQ/dV) vs. potential plots of a) LNMO b) 3:1, 1:1, 1:3 LNMO/Gr hybrid cathodes, and c) graphite (three-electrode configuration; RE: Li metal; CE: LTO; Electrolyte: HCE).

Charge/discharge rate capability investigations

Figure 5(a) displays relative discharge energies depending on the C-rate. 3:1 and 1:3 hybrid cathodes show inferior results whereas the 1:1 hybrid cathode delivers the highest relative energies up to 2 C, thus indicating an impact of the material ratio and a possible synergistic effect. At high potentials graphite maintains its capacity the best. As depicted in Figure 5(b), LNMO delivers the highest specific discharge energies due to its high specific capacity up to 1 C. From 2 C upwards, the 1:1 hybrid cathode shows comparable values to LNMO, presumably combining the high specific capacity of LNMO and the rate capability of graphite as seen in Figure 5(a). These results suggest that a mixture of these materials synergistically exceeds the performance of its base materials. Heubner *et al.* recently showed, in the context of LiMn₂O₄ (LMO)/LFP hybrid cathodes for LIBs, that the electric parallel

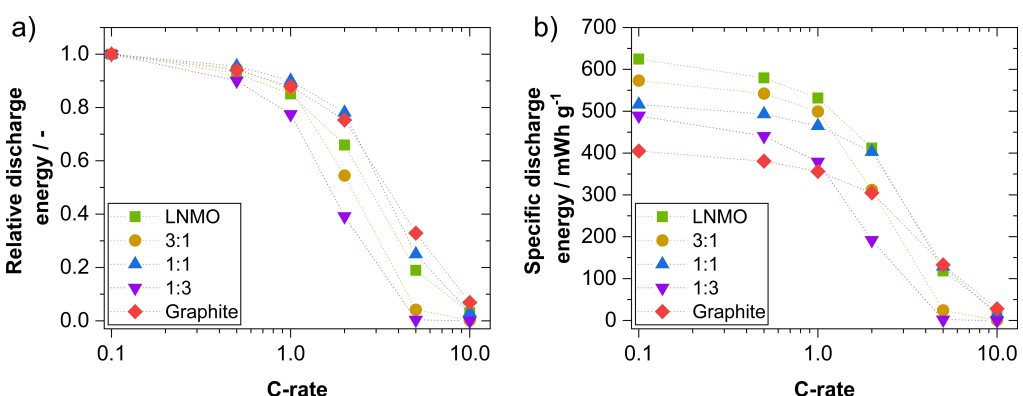


Figure 5. a) Relative and b) specific discharge energies of electrodes composed of LNMO, graphite, and the three different LNMO/graphite hybrid cathodes in dependence of the C-rate from charge/discharge rate capability investigations (three-electrode configuration; half-cell setup; RE: Li metal; CE: LTO) with HCE. Potential range: 3.4–5.0 V vs. Li|Li⁺.

connection of the components allows the applied current to be distributed in a way that the voltage losses become minimal.^[28] Particularly, a high-resistance component can contribute to the capacity of the hybrid electrode at C-rates that exceed its rate capability by carrying smaller currents, whereby the low-resistance component accommodates higher currents than the applied one. If the additional capacity contribution of the high-resistance component overcompensates the capacity losses of the low-resistance component that are caused by the higher effective current, the sum of the components' capacities can be larger than expected from the weighted superposition. The results in Figure 5 suggest a similar synergistic effect in 1:1 LNMO/Gr hybrid cathodes.

Reaction sequence for Li⁺ and PF₆⁻ ion storage in LNMO/Gr hybrid cathodes

To gain more fundamental insights into the component-specific electrochemical behavior within the hybrid, we used a special experimental setup including a model-like hybrid cathode (MLHC), which allows a direct recording of the electrochemical interactions between the components. The experimental setup used to unfold the component-specific electrochemical behavior was described and validated comprehensively in the context of hybrid anodes and cathodes for LIBs.^[29,30] Briefly stated, the different active materials in the hybrid cathode are short-circuited by physical contact, conductive additives, or the current collector foil. This is thermodynamically like having separate electrodes short-circuited by a low-resistance connection. Based on this consideration, we use separate but short-circuited single-component electrodes to form a MLHC. Figure 6(a) depicts schematics of the cell design and the electric network for recording the individual electrochemical behaviors of the components in the MLHC. The cathode holder is made of PCTFE (CF₂CCIF)_n, provided with four electrically insulated current collectors. Assembling of the cell is done by placing single component LNMO and Gr electrodes in the working electrode holder, which are then shorted externally via low-

impedance ammeters to form the MLHC. This allows deconvolution of the component specific currents during battery cell cycling and observation of any internal dynamics among LNMO and Gr. Component specific discharge capacities and Coulombic efficiencies are shown in Figure S2.

Figure 6(b) shows component specific currents and corresponding redox activities during charging (C/10) and discharging (C/10) of an MLHC consisting of LNMO/Gr (1:1 m/m). In this case, the term 'redox activity' describes the shares of Li⁺-(de)insertion in LNMO and PF₆⁻-(de)intercalation in Gr, respectively, in the total current applied to the cell. During operation, several SOC or voltage regions can be sequentially identified where one component dominates (green for LNMO, red for Gr in the color code in Figure 6b) or both contribute to the electrode reaction (white in the color code in Figure 6b). For example, at the very beginning of charging, the electrode reaction is dominated by Li⁺-extraction from LNMO followed by almost sole PF₆⁻-intercalation into Gr. Afterwards, both Li⁺-extraction and PF₆⁻-intercalation take place simultaneously. At medium SOC, LNMO dominates the electrode reaction, while Gr is again the main contributor at high SOC during charge. The redox activity of the components during discharging is basically a mirror image of the charging process. Small deviations from this behavior are most likely caused by different overpotentials of Li⁺-(de)insertion in LNMO and PF₆⁻-(de)intercalation into Gr, respectively.

The investigations using the MLHC further allow to estimate the component specific change in stoichiometry based on the consumed electric charge. Figure 6(c and d) depicts the Li⁺ content in LNMO and the PF₆⁻ content in Gr depending on the cell voltage (Figure 6c) and the SOC (Figure 6d). Li⁺-(de)insertion in LNMO mostly occurs around 4.7 V vs. Li|Li⁺, representing the reactions of Ni²⁺|Ni³⁺ and Ni³⁺|Ni⁴⁺.^[27] In contrast, the PF₆⁻ content in Gr changes more continuously over the voltage window of 4–5 V vs. Li|Li⁺, representing the superposition or 'blurry' transition of staging phenomena as described above. The voltage hysteresis between charging and discharging is larger for Gr than for LNMO. Again, this behavior is most likely caused by different overpotentials of Li⁺

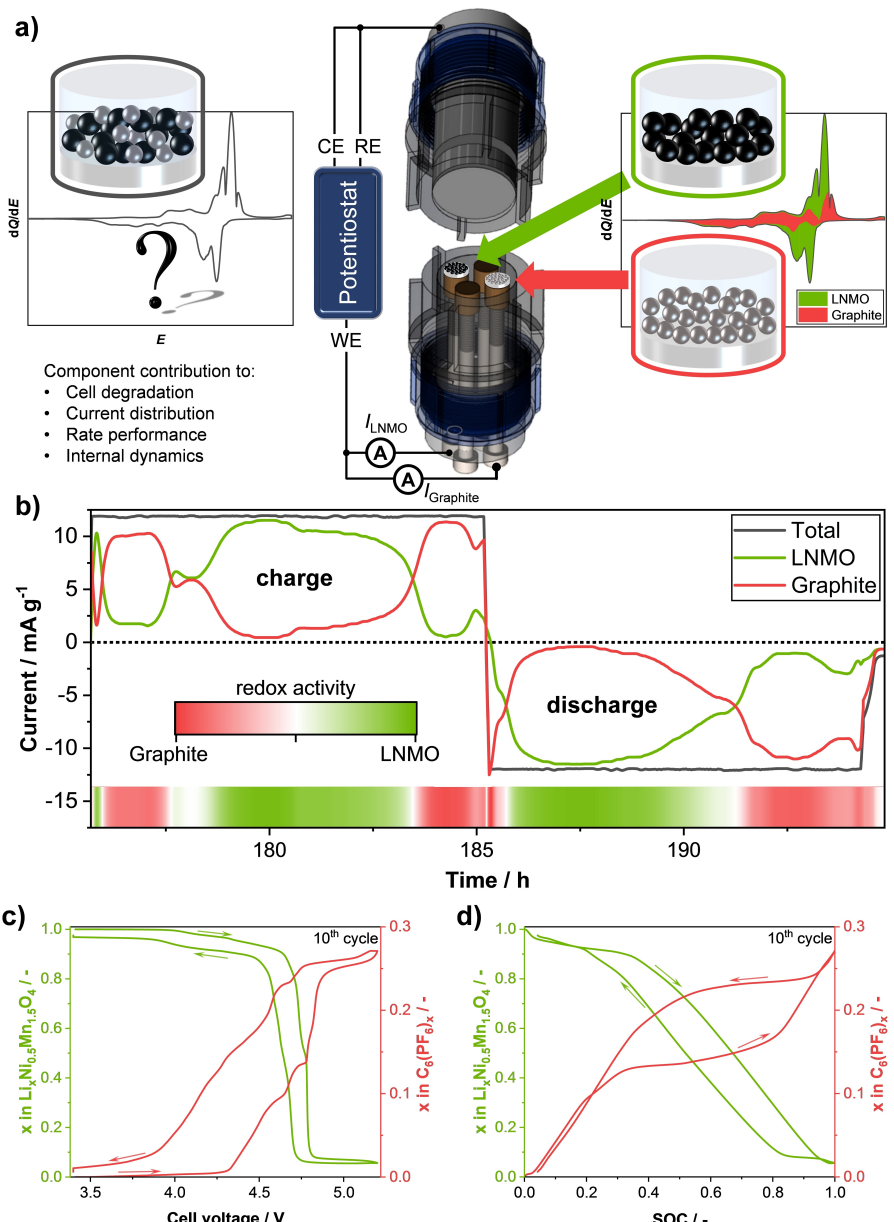


Figure 6. a) Schematic representation of the segmented cell approach: Single component electrodes are connected in parallel serving as joint working electrode in an electrochemical cell. External shorting via low-impedance ammeters forms a model-like hybrid cathode (MLHC) that allows deconvolution of the component specific charging and discharging currents during operation and observation of any internal dynamics among the components. b) Component specific currents and redox activity during charging and discharging of the hybrid cathode at C/10. c, d) Component specific change in stoichiometry derived from the consumed electric charge plotted against electrode voltage (c) and SOC (d).

-(de)insertion into LNMO and PF_6^- -(de)intercalation into Gr, respectively. While the potential dependence of the redox activity should be independent from the composition of the hybrid cathode, the SOC dependence will change with increasing LNMO and Gr content, respectively. For the investigated 1:1 hybrid cathode, the main redox activity of LNMO occurs at $0.2 < \text{SOC} < 0.8$ (Figure 6d). In this SOC region, the PF_6^- content in Gr is almost constant. In contrast, for $0.2 > \text{SOC} > 0.8$, the Li^+ content in LNMO hardly changes, while PF_6^- -(de)intercalation in Gr dominates the electrode reaction resulting in a GIC composition of $(\text{PF}_6)\text{C}_{24}$ at 5.0 V and $(\text{PF}_6)\text{C}_{22}$ at 5.2 V (see Table S3). Overall, the redox activity derived from the compo-

nent specific currents agrees with the results of the dQ/dV vs. potential analysis (Figure 4).

The specific redox potential (ranges) of LNMO and Gr are quite close to each other and partially overlap. In contrast, Hao *et al.*^[19] designed LFP/graphite electrodes that have widely separated redox potentials. Li^+ -(de)intercalation in LFP occurs at ~ 3.45 V vs. $\text{Li}^+/\text{Li}^{+}$, whereas PF_6^- -(de)intercalation in Gr occurs mainly at ~ 4.5 V vs. $\text{Li}^+/\text{Li}^{+}$. Consequently, the Li^+ and PF_6^- intercalating components are not charged and discharged simultaneously but one after another in the LFP/Gr composite. At low SOC, the entire current is consumed by the LFP while at high SOC, solely PF_6^- -(de)intercalation into/from Gr takes place.

Accordingly, the effective C-rate (or specific current in mA g^{-1}) applied to the components is higher than the nominal one, which is related to the capacity or mass of the entire electrode. These permanently higher loads can reduce rate capability and cycling stability of the LFP/Gr electrode.^[30] The material combination LNMO/Gr and resulting overlap of redox activities shown here is very advantageous in this respect.

To verify the reaction mechanism derived from the segmented cell experiment, *operando* XRD analysis has been performed for the first several cycles at the synchrotron facility ALBA (Barcelona, Spain). An *in situ* cell with a 1:1 LNMO/Gr hybrid cathode was charged and discharged with C/5 for the first several cycles between 3.5–5 V vs. Li|Li⁺. Figure 7(a) shows a waterfall-plot of two selected angle regions during cycling, enabling monitoring the (002) reflection of Gr and (311) reflection of LNMO. Upon charging and discharging, changes in the reflection positions of LNMO and Gr, pointing at their redox activity, occur at different cell voltages.

Structural evolution of LNMO upon Li⁺-removal and reinsertion in the 1:1 hybrid cathode confirms results from the

literature.^[31] It is known that LNMO features a reversible two-step delithiation mechanism in LIB cells, corresponding to a solid-solution process in the first step at ~4.55 V, and a two-phase process with a plateau at ~4.75 V. These phase transitions are attributed to the redox couples Ni²⁺|Ni³⁺ and Ni³⁺|Ni⁴⁺.^[27] Sometimes an additional process at ~4.0 V is observed as well, reflecting a redox activity of the Mn³⁺|Mn⁴⁺ pair due to some oxygen deficiency in the spinel material.^[31,32] In our experiment, upon Li-removal from the hybrid 1:1 cathode, cubic LNMO first shows a lattice shrinkage, corresponding to a solid-solution reaction mechanism at a cell voltage of 4.5 V, which occurs, however, at the SOC-value of already 0.35. Therefore, graphite starts to intercalate PF₆⁻ anions prior to the redox activity of LNMO. Above 4.8 V, appearance of a second isostructural LNMO spinel phase with a much smaller lattice parameter a (Li-poor phase) can be concluded (Figure 7b) due to the splitting of the (311) reflection. During further Li-extraction, cell metrics of both phases do not change anymore with the Li-content, reflecting a classical two-phase reaction mechanism. The subsequent dis-

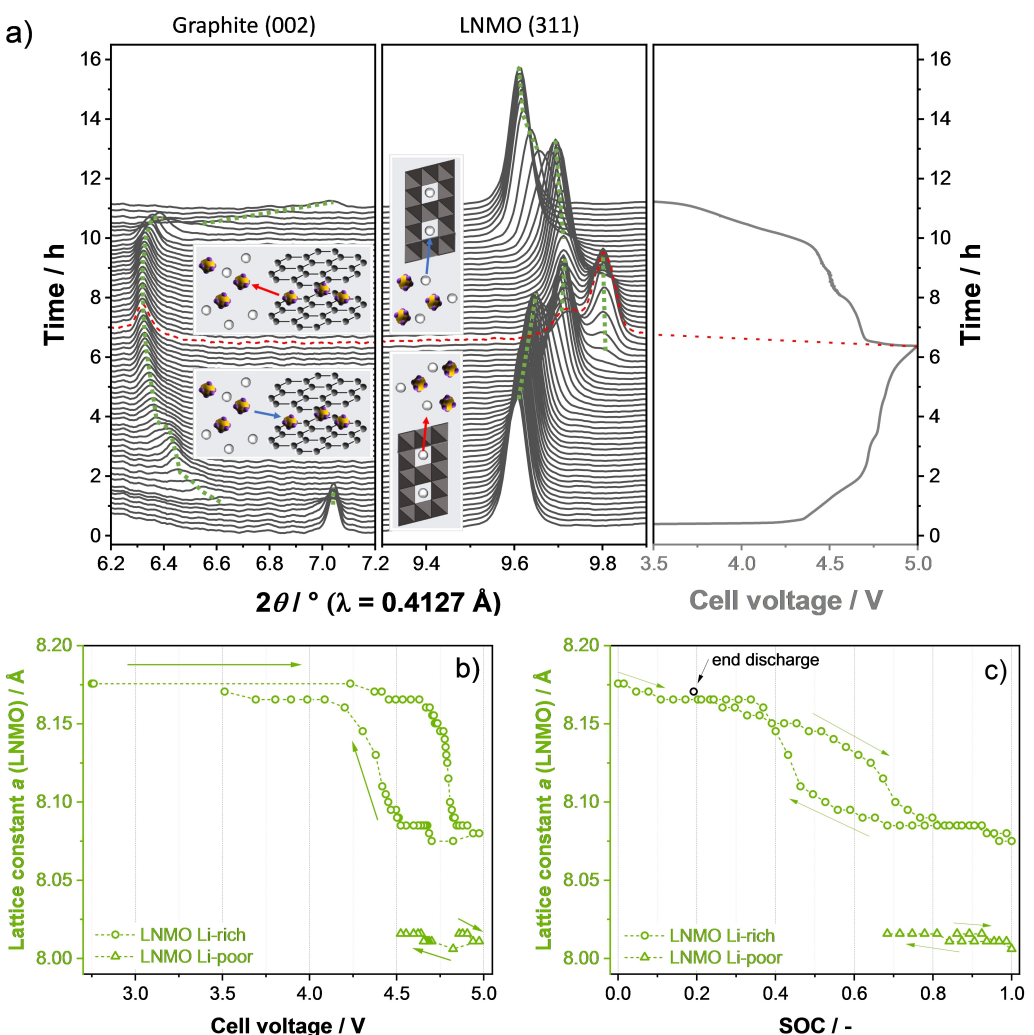


Figure 7. *Operando* XRD measurements of the 1:1 LNMO/Gr hybrid cathode during cycling (C/5) between 3.5–5.0 V. a) Waterfall-plot of two selected angle regions 6.2–7.2° 2θ and 9.3–9.9° 2θ. Lattice constants calculated from *operando* XRD results for LNMO vs. b) cell voltage and c) state-of-charge.

charging process is mostly reversible: during discharging, no substantial changes were observed to 4.65 V. Between 4.65 and 4.5 V, re-distribution in intensity of both (311) reflections and disappearance of the one at a higher 2θ value implies a change from the two-phase reaction mechanism to a solid-solution mechanism. Between 4.5 V and 4.25 V, the lattice parameter of the Li-rich LNMO is varying with the Li-content, while remains constant below 4.25 V. The SOC value of 0.4 at 4.25 V again points to a redox activity of graphite below this cell voltage. Note that some hysteresis in the evolution of the lattice parameter of the Li-rich LNMO phase was detected (Figure 7b, c).

In the case of graphite, intercalation of species between layers in a two-dimensional structure results either in appearance of additional Bragg reflections in diffractograms pointing to some staging process, or exfoliation and/or structural collapse, leading to complete disappearance of Bragg reflections of the initial phase. The appearance of two new $(00n+1)$ and $(00n+2)$ peaks is a clear indication of staging, meaning that the intercalated species are present only in each n^{th} space between the graphite sheets. The periodic repeat distance (l_c), the intercalant gallery height (d) and the gallery expansion (Δd) can be used to describe the lattice expansion as shown in Equation (4).^[14,21,23,33]

$$l_c = d_i + 3.35 \text{ \AA} \cdot (n - 1) = \Delta d + 3.35 \text{ \AA} \cdot n < + \quad (4)$$

The stage number n [Equation (5)] and the distance between two graphite sheets with intercalated molecules [d_s , gallery height; Equation (6)] can be calculated from the position of two neighboring reflections $(00n+1)$ and $(00n+2)$ as

$$n = \frac{1}{\left[1 - \left(\frac{\sin \theta_{00(n+1)}}{\sin \theta_{00(n+2)}} \right) \right] - 2} \quad (5)$$

$$c_n = (n - 1)c_0 + d_s = \lambda \cdot n / [2 \sin \theta_{00n}] \quad (6)$$

where c_0 – the distance between two neighboring graphitic layers, corresponding to the half of the lattice parameter c of graphite, c_n – the repeating distance after intercalation. Depending on the nature of intercalated ions A, ordered hexagonal superstructures can occur with the compositions AC_6 , AC_8 , AC_{14} , AC_{18} , etc. Since intercalated anions are mostly complex and contain more than one atom (PF_6^- , BF_4^- , ClO_4^-), their intercalation/deintercalation into/from graphite is much more kinetically hindered than Li^+ ion insertion/extraction into/from the 3D LNMO structure.

During charging of the 1:1 hybrid cathode, the (002) reflection of graphite at $7.04^\circ 2\theta$ remains constant up to 4.3 V. At 4.4 V, the reflection intensity decreases, followed by an abrupt change of the reflection position to $6.6^\circ 2\theta$ at 4.5 V, which marks the beginning of the PF_6^- intercalation. Above 4.75 V, no changes in reflection position and intensity were observed, indicating a completed staging process. The stage of the GIC in the hybrid cathode at the end of charging (C/5; 5.0 V) was calculated via equation (5) to be $n=1.81$, meaning stage 2

formation is completed and further intercalation took place. Additionally, (in situ) Raman measurements were conducted on the raw materials as well as on the electrodes, complementarily confirming anion intercalation while charging (Figures S4 and S5). Upon discharging, the graphite reflection at $6.31^\circ 2\theta$ does not change up to 4.5 V. Between 4.5 and 4.4 V, its intensity decreases abruptly, followed by a shift to higher 2θ , indicating PF_6^- extraction from the graphite structure, which is completed at 3.5 V. The (002) reflection of graphite after the first PF_6^- -insertion/extraction process is less-intensive and notably broadened, pointing a noticeable structural disorder. These results partially contradict the behavior observed in the MLHC experiments (Figure 6), where Gr is still active during charging at high cell voltage, while the reaction of LNMO becomes negligible due to Li depletion in the lattice.

To understand these inconsistencies, additional potentiodynamic *in situ* XRD measurements at a scan rate of 0.05 mVs^{-1} (comparable to C/10) were performed on graphite, LNMO and 1:1 LNMO/Gr hybrid electrodes using an in-house diffractometer (see Figure S3). The graphite part of the hybrid electrode completed stage 2 formation (1.74) upon charging to 5.0 V and stage 1 formation at 5.1 V (see Table S4). Considering the lower charging current, both synchrotron and in-house measurements show similar results for the staging behavior at 5.0 V. Only when charging the 1:1 hybrid cathode to higher voltages (5.1 V), stage 1 is reached. This leads on one hand to higher capacity and on the other hand to redox activity at high cell voltages, which is in very good agreement with the MLHC experiments (see Figure 6b). Measuring the pure Gr electrode, we observed the same staging behavior (reflection positions) as in hybrid electrodes but occurring at lower voltages shifted by $\geq 0.1 \text{ V}$ (see Table S4). This implies that utilizing Gr in hybrid electrodes increases graphite's charge potential while simultaneously decreasing LNMO's charge potential. The discharge voltages behave in the opposite manner so the voltage efficiency of LNMO in the hybrid electrode is increased, while of Gr it is decreased (Figure S3). This corroborates the assumption that LNMO and graphite interact with each other.

Battery cell testing and modeling

Initial measurements and investigations of the working principle of LNMO/Gr hybrid cathodes were carried out with electrodes of low areal capacities, as typically used in research on battery materials. To evaluate whether battery cells with hybrid cathodes have advantages over comparable LIBs and DIBs, further investigations were carried out applying higher areal capacities. Due to the results of the MLHC, the mass fractions of LNMO and Gr were changed to match their absolute capacity (1:1 Q/Q), resulting in a 1:1.36 (m/m) hybrid cathode. Figure 8 shows SEM images and EDS mappings of the cross-section of a hybrid cathode (1:1.36 m/m) with an areal capacity of 2 mAh cm^{-2} . The LNMO particles, represented by Mn, Ni and O in the EDS mapping, are homogeneously distributed in a matrix of graphite, binder, and conductive carbon, represented by C in the EDS mapping. The geometric porosity of this electrode is

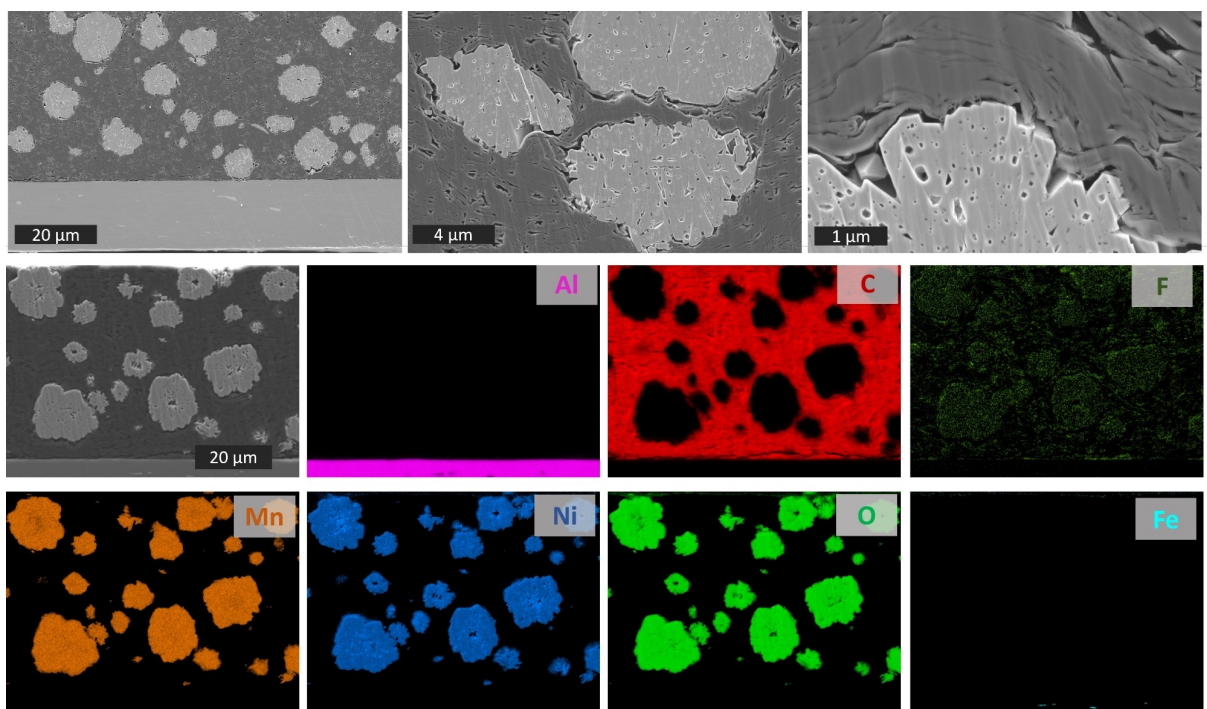


Figure 8. Cross-sectional SEM images (top row) and EDS mappings (bottom rows) of a 1:1.36 LNMO/Gr hybrid cathode.

calculated to 20%, although it appears much lower in the SEM images. Comparable SEM/EDS analyses of pure LNMO and pure Gr electrodes are provided as Supporting Information (Figures S6 and S7).

The rate capability of LIB electrodes with high areal capacity is typically limited by Li^+ diffusion in the electrolyte within the electrode pores.^[7,8] By introducing a second electroactive species (anions), we expect the hybrid cathodes to have notably higher rate capability than pure LNMO or Gr electrodes of similar design. The rate capability of hybrid cathodes, pure

LNMO and pure Gr electrodes was investigated by chronoamperometric measurements.^[34] Figure 9(a) shows the relative capacity as a function of the C-rate, calculated from the chronoamperometric response (voltage step to 5.0 V). In contrast to our expectations the rate capability decreases in the series: 1) pure LNMO cathode (LIB), 2) pure graphite cathode (DIB), 3) hybrid cathode. To better understand why our assumptions of an improved rate capability of the hybrid cathode do not hold true in the experiments conducted, some simple model considerations were carried out. The modelling is

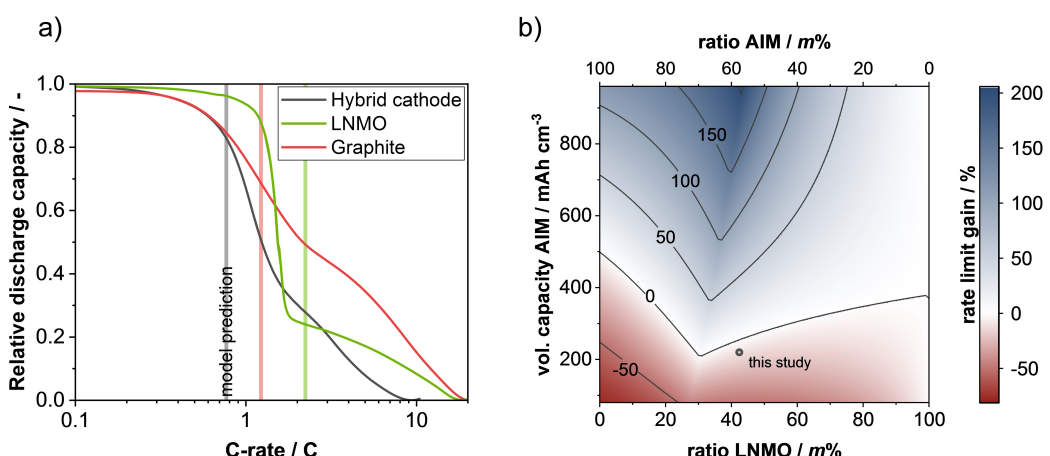


Figure 9. a) Relative discharge capacity of capacity balanced LNMO/Gr hybrid cathode as a function of the C-rate compared to pure LNMO and Gr electrodes of similar design. The vertical lines represent the diffusion limiting C-rate (DLC) predicted for the different electrodes (see Supporting Information for details). b) Predicted gain in the rate limit of LNMO/Gr hybrid electrodes with respect to a pure LNMO electrode of same areal capacity depending on the composition and the volumetric capacity of graphite.

based on the concept of the so-called diffusion-limited C-rate (DLC).^[8,35] In brief, this model assumes that electrolyte diffusion in the pores of the electrodes is the limiting process at high rates. For currents higher than the DLC, a massive depletion of Li⁺ ions takes place in the electrolyte within the electrode pores and the intercalation reaction comes to a halt. Consequently, the extractable capacity decreases, which has been confirmed many times for electrodes with capacities $> 2 \text{ mAh cm}^{-2}$.^[36] The DLC depends on the electrolyte and active material properties as well as the thickness, porosity and tortuosity of the electrode. To predict the rate limit of hybrid cathodes, the DLC concept has been extended to include the contribution of the anions to the intercalation current/capacity (see Section S7 in Supporting Information for details). Reference parameters used for the calculation of the DLC are shown in Table S5. Figure 9(a) displays that the predicted rate limit (DLC) of the hybrid cathodes is indeed lower than that of pure graphite and pure LNMO electrodes, which agrees with the experimental results. It is noticeable that the LNMO capacity drops considerably at C-rates $> 1\text{C}$, most likely caused by diffusion limitation in the pore electrolyte. A great advantage of hybrid cathodes is the intrinsically high electronic conductivity caused by the incorporation of graphite. The conductivity of the Gr electrodes is twice that of LNMO, while the conductivity of the hybrid cathodes is in between (see Figure S8).

To better understand this unexpected behavior, a parameter study has been conducted. The gain in rate capability compared to pure LNMO was determined as a function of the volumetric capacity of the anion intercalating material (AIM) and its mass ratio in the hybrid cathode (Figure 9b). The specific capacities and densities based on volumetric capacity used for this parameter study are shown in Figure S9. The rate capability increases with increasing volumetric capacity of the AIM. The composition dependence is more complex, showing a local maximum at intermediate compositions, which slightly shifts to higher LNMO fractions with increasing volumetric capacity of the AIM. These dependencies are closely related to the electrode design. The higher the volumetric capacity of the AIM, the thinner the electrode for the same areal capacity, which decreases the diffusion length and thus increases the rate capability. If the volumetric capacity of the AIM is smaller than the one of LNMO, hybrid electrodes of the same areal capacity will always be thicker than pure LNMO electrodes, which increases the diffusion length. At a certain composition/thickness, the increase in diffusion length overcompensates the benefits of the hybrid concept (two diffusing species) and the rate capability becomes inferior to pure LNMO electrodes. If the AIM has a volumetric capacity notably higher than for LNMO, the rate limit gain is positive for any composition. Accordingly, LNMO/Gr hybrid cathodes do not have intrinsically higher rate capability compared to LIB or DIB cathodes but must meet certain material and design requirements in order for synergistic effects to occur. Figure 9(b) also shows the predicted gain in rate capability for the LNMO/Gr hybrid cathode produced in this work. Obviously, in this case the conditions for achieving synergistic effects are not met, so that the rate capability of the hybrid cathode is lower than that of a pure LNMO electrode,

which agrees with the experimental findings (Figure 9a). Based on our estimations, with LNMO as the Li intercalation material, the AIM would have to have a volumetric capacity $> 260 \text{ mAh cm}^{-3}$ (e.g., $> 130 \text{ mAh g}^{-1}$ and 2 g cm^{-3}) to make synergy effects possible.

Conclusions

An LNMO/Gr hybrid cathode concept based on Li⁺ ion storage in LNMO and PF₆⁻ anion storage in graphite is proposed, combining the advantages of dual-ion and Li ion batteries. The cell voltage profile, specific capacity and cycling stability and are highly sensitive to both, the mass ratio of LNMO and Gr in the hybrid cathode as well as the used electrolyte. A highly concentrated electrolyte, adapted from DIB research, is found to provide the most beneficial electrochemical properties, which is mainly caused by the lowering of the PF₆⁻-intercalation potential and increased specific capacity of graphite. While pure LNMO electrodes provide the highest energy density at low rates and pure Gr exhibits excellent rate capability, the 1:1 LNMO/graphite hybrid cathode is intermediate in energy density (as expected) but shows a synergistic effect in terms of rate capability. Investigations of the reaction mechanism show the SOC dependent reaction distribution between Li⁺-(de)intercalation in LNMO and PF₆⁻-(de)intercalation in Gr, which was confirmed by *operando* XRD and *in situ* Raman measurements. In contrast to our expectations, battery cells with LNMO/Gr hybrid cathodes of higher areal capacity show lower rate capability than comparable LIBs and DIBs. Simple modeling shows that the anion intercalating materials must provide certain properties to achieve synergistic effects in hybrid cathodes. Based on our estimations, with LNMO as the Li⁺ storing material, the anion intercalating material would have to have a specific volumetric capacity of $> 260 \text{ mAh cm}^{-3}$ to make synergy effects possible. Even if this requirement was not fulfilled here, the results provide a pioneering basis for the development of novel hybrid concepts. This will open a wide range of new combination possibilities in the field of conventional and post-Li battery technologies. The Li-based hybrid approach shown here could be extended to cells with metallic anodes, whereby materials with even notably higher volumetric energy density than Li, Na and K, such as Al and Mg, could be used. In this respect, the presented insights lay the foundation for a completely new type of battery with potentially very advantageous properties in terms of cost, availability of raw materials, environmental friendliness, recyclability, and electrochemical performance.

Experimental Section

Electrode preparation

LiNi_{0.5}Mn_{1.5}O₄ (LNMO, BASF SE), graphite (Gr, Timrex® KS6 Primary Synthetic Graphite, Imerys Graphite & Carbon), Li₄Ti₅O₁₂ (LTO, Johnson Matthey Catalysts) and different LNMO/Gr mixtures were used for the electrode preparation with conductive additive (C-nergy™ Super

C65, Imerys Graphite & Carbon) and polyvinylidene fluoride (PVdF, Solvay Solef® 5130) as binder. LNMO electrodes, graphite electrodes, and three different LNMO/graphite hybrid electrodes were prepared in a ratio of 90 m% active material to 5 m% conductive carbon and 5 m% binder. First, conductive carbon, PVdF and the active material were dry mixed using a swing mill (Retsch MM400) for 15 min at 15 Hz. Then, the electrode powder was suspended with NMP and mixed for 30 min at 20 Hz and finally for 60 min at 30 Hz. Electrode pastes were coated on an Al foil (20 µm) with a doctor blade, dried at 80 °C for 24 h and then calendered to achieve the targeted porosity of 40%. The parameters of the electrodes prepared are provided in Table S1. For later investigations, cathodes with a higher areal capacity (>1.5 mAh cm⁻²) were produced, whereby the mass fractions of LNMO and Gr in the hybrid cathode were adjusted to 1:1.36 m/m to obtain a capacity balanced electrode (1:1 Q/Q). Li₄Ti₅O₁₂ electrodes were prepared using LTO (87.4 m%), conductive agent (8 m%) and PVdF (4.6 m%) and were mixed and dispersed in NMP (1.44 g NMP per 1 g solid content). The paste was coated on Al foil using a doctor blade. Circular electrodes with a diameter of 12 mm and a thickness of approximately 107 µm were punched out and dried at 80 °C under vacuum. An average mass loading of 16.5±0.6 mg cm⁻² was obtained.

Electrochemical characterization

Electrode discs with a diameter of 12 mm were punched out and dried at 80 °C under reduced pressure before being transferred to a dry room for cell assembly. All electrochemical measurements for the initial characterization were conducted with at least three electrodes of each material. Therefore, diagrams show mean values and for cycling plots including error bars. For cycling investigations, two-electrode coin cells (CR2032, Hohsen Corporation) were used. Positive electrodes ($\varnothing=12$ mm) of various LNMO/Gr hybrid cathodes were employed, whereas Li metal (99.9%, Aldrich) was used as the negative electrode ($\varnothing=15$ mm). The separator consisted of polypropylene fiber (Freudenberg FS2226, 6-layers) soaked with 150 µL of basic electrolyte (BE, ethylene carbonate (EC):ethyl methyl carbonate (EMC), 3:7 m/m, 1 M LiPF₆ (BASF)) and highly concentrated electrolyte (HCE, 4 M LiPF₆ in dimethyl carbonate (DMC)), respectively. Electrochemical experiments were performed using a MacCor Series 4000 automated test system (MacCor Inc.). A charge/discharge rate of 0.5 C was applied after three formation cycles at 0.1 C in a cell voltage range from 3.4 to 5.0 V. A rest step of five minutes was applied after each cycle. Three 'check-up' cycles at 0.1 C were conducted each 100 cycles. Constant current rate capability investigations were conducted in a potential range of 3.4 to 5.0 V vs. Li|Li⁺ using three-electrode T-type Swagelok® cells with Li metal as reference electrode (RE, $\varnothing=8$ mm), LNMO/Gr as working electrode (WE) and Li₄Ti₅O₁₂ (LTO) as counter electrode (CE, $\varnothing=12$ mm). The charge/discharge rate varied from 0.1 C to 10 C. Theoretical capacities of hybrid electrodes were determined by mass weighted summation of the theoretical capacities of the pure materials (LNMO: 147 mAh g⁻¹; Gr: 100 mAh g⁻¹ for ~PF₆C₂₂ stoichiometry).^[14]

Materials characterization

The electrodes were analyzed by scanning electron microscopy (SEM; NVision40, Zeiss). The cross-sectional preparation of the electrodes was performed using the broad ion preparation method (TIC020, Leica). Operando X-ray measurements were performed at the synchrotron facility ALBA (Barcelona, Spain).^[37] Structural characterizations of the 1:1 LNMO/Gr hybrid cathode in Li metal cells were carried out using synchrotron radiation ($\lambda=0.4127$ Å) in

transmission mode at the powder diffraction beam line BL04-MSPD. The cells were installed in an eight-fold coin cell holder connected to a Biologic Instruments potentiostat, which was applied as described in Herklotz *et al.*^[38] The data were collected in 0.006° steps over the 2θ-range from 0.55° to 59.19°. Additionally, LNMO, graphite and the 1:1 hybrid cathode were investigated via *in-situ* XRD and (*in situ*) Raman spectroscopy (see Supporting Information).

Supporting Information

The authors have cited additional references within the Supporting Information.^[39]

Acknowledgements

The authors wish to thank the Ministry of Economic Affairs, Innovation, Digitalization and Energy of the State of North Rhine-Westphalia (MWIDE) for funding this work in the project "GrEEn" (313-W044 A). We also thank Andre Bar for his graphical support. The authors acknowledge Dr. A. Missyul (ALBA synchrotron, Barcelona, Spain) for the help during *operando* XRD experiments performed at BL04-MSPD beamline at ALBA Synchrotron. Open Access funding enabled and organized by Projekt DEAL.

Conflict of Interests

The authors declare no conflict of interest.

Data Availability Statement

The data that support the findings of this study are available from the corresponding author upon reasonable request.

Keywords: hybrid cathode • dual-ion batteries • Li ion batteries • high voltage • high power

- [1] a) M. Li, J. Lu, Z. Chen, K. Amine, *Adv. Mater.* **2018**, *30*, 1800561; b) J. Xie, Y.-C. Lu, *Nat. Commun.* **2020**, *11*, 2499; c) A. Masias, J. Marcicki, W. A. Paxton, *ACS Energy Lett.* **2021**, *6*, 621; d) R. Schmuck, R. Wagner, G. Hörpel, T. Placke, M. Winter, *Nat. Energy* **2018**, *3*, 267; e) M. Marinaro, D. Bresser, E. Beyer, P. Faguy, K. Hosoi, H. Li, J. Sakovica, K. Amine, M. Wohlfahrt-Mehrens, S. Passerini, *J. Power Sources* **2020**, *459*, 228073.
- [2] S. Dünen, J. Betz, M. Kolek, R. Schmuck, M. Winter, T. Placke, *Small Methods* **2020**, *4*, 2000039.
- [3] a) X.-G. Yang, T. Liu, C.-Y. Wang, *Nat. Energy* **2021**, *6*, 176; b) F. Zou, H. C. Nallan, A. Dolocan, Q. Xie, J. Li, B. M. Coffey, J. G. Ekerdt, A. Manthiram, *Energy Storage Mater.* **2021**, *43*, 499; c) W. Li, E. M. Erickson, A. Manthiram, *Nat. Energy* **2020**, *5*, 26.
- [4] H. Cheng, J. G. Shapter, Y. Li, G. Gao, *J. Energy Chem.* **2021**, *57*, 451.
- [5] C. Heubner, K. Voigt, P. Marcinkowski, S. Reuber, K. Nikolowski, M. Schneider, M. Partsch, A. Michaelis, *Adv. Energy Mater.* **2021**, *11*, 2102647.
- [6] a) C. Heubner, A. Nickol, J. Seeba, S. Reuber, N. Junker, M. Wolter, M. Schneider, A. Michaelis, *J. Power Sources* **2019**, *419*, 119; b) Y. Kuang, C. Chen, D. Kirsch, L. Hu, *Adv. Energy Mater.* **2019**, *9*, 1901457.

- [7] C. Heubner, K. Nikolowski, S. Reuber, M. Schneider, M. Wolter, A. Michaelis, *Batteries & Supercaps* **2021**, *4*, 268.
- [8] C. Heubner, M. Schneider, A. Michaelis, *Adv. Energy Mater.* **2020**, *10*, 1902523.
- [9] a) T. Danner, M. Singh, S. Hein, J. Kaiser, H. Hahn, A. Latz, *J. Power Sources* **2016**, *334*, 191; b) H. Zheng, J. Li, X. Song, G. Liu, V. S. Battaglia, *Electrochim. Acta* **2012**, *71*, 258.
- [10] M. Weiss, R. Ruess, J. Kasnatscheew, Y. Levartovsky, N. R. Levy, P. Minnmann, L. Stoltz, T. Waldmann, M. Wohlfahrt-Mehrens, D. Aurbach et al., *Adv. Energy Mater.* **2021**, *11*, 2101126.
- [11] a) T. Placke, P. Bieker, S. F. Lux, O. Fromm, H.-W. Meyer, S. Passerini, M. Winter, *Zeitschrift für Phys. Chemie* **2012**, *226*, 391; b) X. Zhou, Q. Liu, C. Jiang, B. Ji, X. Ji, Y. Tang, H.-M. Cheng, *Angew. Chem. Int. Ed.* **2020**, *59*, 3802; c) Z. Guo, Z. Xu, F. Xie, J. Feng, M. Titirici, *Adv Energy Sustain. Res.* **2021**, *2*, 2100074; d) K. V. Kravchyk, M. V. Kovalenko, *Adv. Energy Mater.* **2019**, *9*, 1901749.
- [12] T. Placke, O. Fromm, S. F. Lux, P. Bieker, S. Rothermel, H.-W. Meyer, S. Passerini, M. Winter, *J. Electrochem. Soc.* **2012**, *159*, A1755-A1765.
- [13] T. Placke, A. Heckmann, R. Schmuck, P. Meister, K. Beltrop, M. Winter, *Joule* **2018**, *2*, 2528.
- [14] T. Placke, G. Schmuelling, R. Kloepsch, P. Meister, O. Fromm, P. Hilbig, H.-W. Meyer, M. Winter, *Z. Anorg. Allg. Chem.* **2014**, *640*, 1996.
- [15] X. Ou, D. Gong, C. Han, Z. Liu, Y. Tang, *Adv. Energy Mater.* **2021**, *11*, 2102498.
- [16] W. Wang, H. Huang, B. Wang, C. Qian, P. Li, J. Zhou, Z. Liang, C. Yang, S. Guo, *Sci. Bull.* **2019**, *64*, 1634.
- [17] H. Chen, F. Guo, Y. Liu, T. Huang, B. Zheng, N. Ananth, Z. Xu, W. Gao, C. Gao, *Adv. Mater.* **2017**, 1605958.
- [18] a) Y. Sui, C. Liu, R. C. Masse, Z. G. Neale, M. Atif, M. AlSalhi, G. Cao, *Energy Storage Mater.* **2020**, *25*, 1; b) M. Greenwood, J. M. Wrogemann, R. Schmuck, H. Jang, M. Winter, J. Leker, *J. Power Sources Adv.* **2022**, *14*, 100089.
- [19] J. Hao, F. Yang, S. Zhang, H. He, G. Xia, Y. Liu, C. Didier, T. Liu, W. K. Pang, V. K. Peterson et al., *Proc. Nat. Acad. Sci.* **2020**, *117*, 2815.
- [20] a) R. Santhanam, B. Rambabu, *J. Power Sources* **2010**, *195*, 5442; b) K. Shimoda, M. Murakami, H. Komatsu, H. Arai, Y. Uchimoto, Z. Ogumi, *J. Phys. Chem. C* **2015**, *119*, 13472.
- [21] M. S. Dresselhaus, G. Dresselhaus, *Adv. Phys.* **2002**, *51*, 1.
- [22] W. Zhou, P. H.-L. Sit, *ACS Omega* **2020**, *5*, 18289.
- [23] G. Schmuelling, T. Placke, R. Kloepsch, O. Fromm, H.-W. Meyer, S. Passerini, M. Winter, *J. Electrochem. Soc.* **2013**, *239*, 563.
- [24] S. A. Safran, D. R. Hamann, *Phys. Rev. B* **1980**, *22*, 606.
- [25] A. Heckmann, J. Thienenkamp, K. Beltrop, M. Winter, G. Brunklaus, T. Placke, *Electrochim. Acta* **2018**, *260*, 514.
- [26] a) J. E. Frerichs, L. Haneke, M. Winter, M. R. Hansen, T. Placke, *J. Power Sources Adv.* **2021**, *12*, 100075; b) L. Haneke, J. E. Frerichs, A. Heckmann, M. M. Lerner, T. Akbay, T. Ishihara, M. R. Hansen, M. Winter, T. Placke, *J. Electrochem. Soc.* **2020**, *167*, 140526; c) A. Kotronia, H. D. Asfaw, C.-W. Tai, M. Hahlin, D. Brandell, K. Edström, *ACS Appl. Mater. Interfaces* **2021**, *13*, 3867.
- [27] J. Betz, L. Nowak, M. Winter, T. Placke, R. Schmuck, *J. Electrochem. Soc.* **2019**, *166*, A3531-A3538.
- [28] C. Heubner, T. Liebmann, C. Lämmel, M. Schneider, A. Michaelis, *Batteries & Supercaps* **2022**, *5*, e202100171.
- [29] a) C. Heubner, T. Liebmann, O. Lohrberg, S. Cangaz, S. Maletti, A. Michaelis, *Batteries & Supercaps* **2022**, *5*, e202100182; b) C. Heubner, T. Liebmann, C. Lämmel, M. Schneider, A. Michaelis, *ChemElectroChem* **2018**, *5*, 425.
- [30] T. Liebmann, C. Heubner, C. Lämmel, M. Schneider, A. Michaelis, *ChemElectroChem* **2019**, *6*, 5728.
- [31] M. Yavuz, N. Kiziltas-Yavuz, A. Bhaskar, M. Scheuermann, S. Indris, F. Fauth, M. Knapp, H. Ehrenberg, *Z. Anorg. Allg. Chem.* **2014**, *640*, 3118.
- [32] D. Mikhailova, A. Thomas, S. Oswald, W. Gruner, N. N. Bramnik, A. A. Tsirlin, D. M. Trots, A. Senyshyn, J. Eckert, H. Ehrenberg, *J. Electrochem. Soc.* **2013**, *160*, A3082-A3089.
- [33] W. Rüdorff, E. Schulze, *Z. Anorg. Allg. Chem.* **1954**, *277*, 156.
- [34] C. Heubner, C. Lämmel, A. Nickol, T. Liebmann, M. Schneider, A. Michaelis, *J. Power Sources* **2018**, *397*, 11.
- [35] C. Heubner, S. Reuber, J. Seeba, P. Marcinkowski, K. Nikolowski, M. Schneider, M. Wolter, A. Michaelis, *J. Power Sources* **2020**, *479*, 228704.
- [36] a) H. Gao, Q. Wu, Y. Hu, J. P. Zheng, K. Amine, Z. Chen, *J. Phys. Chem. Lett.* **2018**, *9*, 5100; b) Y. Chen, B. Zhao, Y. Yang, A. Cao, *Adv. Energy Mater.* **2022**, *12*, 2201834; c) M. S. Hossain, L. I. Stephens, M. Hatami, M. Ghavidel, D. Chhin, J. I. G. Dawkins, L. Savignac, J. Mauzeroll, S. B. Schougaard, *ACS Appl. Energ. Mater.* **2020**, *3*, 440; d) J. Kang, M. Atwair, I. Nam, C.-J. Lee, *Energy* **2023**, *125801*; e) F. Wu, M. Liu, Y. Li, X. Feng, K. Zhang, Y. Bai, X. Wang, C. Wu, *Electrochem. Energy Rev.* **2021**, *4*, 382.
- [37] F. Fauth, I. Peral, C. Popescu, M. Knapp, *Powder Diffr.* **2013**, *28*, S360-S370.
- [38] M. Herklotz, J. Weiß, E. Ahrens, M. Yavuz, L. Mereacre, N. Kiziltas-Yavuz, C. Dräger, H. Ehrenberg, J. Eckert, F. Fauth et al., *J. Appl. Crystallogr.* **2016**, *49*, 340.
- [39] a) M. Balabajew, H. Reinhardt, N. Bock, M. Duchardt, S. Kachel, N. Hampp, B. Roling, *Electrochim. Acta* **2016**, *211*, 679; b) D. A. Gómez, J. Coello, S. Maspoch, *Vib. Spectrosc.* **2019**, *100*, 48; c) R. Navratil, A. Kotzianova, V. Halouzka, T. Opletal, I. Triskova, L. Trnkova, J. Hrbac, *J. Electroanal. Chem.* **2016**, *783*, 152; d) M. S. Dresselhaus, A. Jorio, R. Saito, *Annu. Rev. Condens. Matter Phys.* **2010**, *1*, 89; e) Y. Zhu, M. D. Casselman, Y. Li, A. Wei, D. P. Abraham, *J. Electrochem. Soc.* **2014**, *246*, 184; f) M. Kunduraci, J. F. Al-Sharab, G. G. Amatucci, *Chem. Mater.* **2006**, *18*, 3585; g) L. Boulet-Roblin, C. Villevieille, P. Borel, C. Tessier, P. Novák, M. Ben Yahia, *J. Phys. Chem. C* **2016**, *120*, 16377; h) C. Gao, H. Liu, S. Bi, H. Li, C. Ma, *Green Energy & Environ.* **2021**, *6*, 114; i) K. Ariyoshi, Y. Iwakoshi, N. Nakayama, T. Ohzuku, *J. Electrochem. Soc.* **2004**, *151*, A296; j) K. Saravanan, A. Jarry, R. Kostecki, G. Chen, *Sci. Rep.* **2015**, *5*, 8027; k) S. A. Osman, S. S. Ng, Z. Hassan, *J. Phys. Conf. Ser.* **2020**, *1535*, 12029.

Manuscript received: July 4, 2023

Revised manuscript received: July 9, 2023

Accepted manuscript online: July 25, 2023

Version of record online: July 31, 2023